

Distribution of REE between amphibole and pyroxenes in the lithospheric mantle: An assessment from the lattice strain model

CHUNGUANG WANG^{1,*}, YAN LIANG², WENLIANG XU¹, CHENGUANG SUN³, AND KEI SHIMIZU⁴

¹College of Earth Sciences, Jilin University, Changchun 130061, China

²Department of Earth, Environmental and Planetary Sciences, Brown University, Providence, Rhode Island 02192, U.S.A.

³Department of Earth and Planetary Sciences, Jackson School of Geosciences, University of Texas at Austin, Austin, Texas 78712, U.S.A.

⁴WiscSIMS, Department of Geoscience, University of Wisconsin-Madison, Madison, Wisconsin 53706, U.S.A.

ABSTRACT

Amphibole and pyroxenes are the main reservoirs of rare earth elements (REEs) in the lithospheric mantle that has been affected by hydrous metasomatism. In this study, we developed semi-empirical models for REE partitioning between orthopyroxene and amphibole and between clinopyroxene and amphibole. These models were formulated on the basis of parameterized lattice strain models of mineral-melt REE partitioning for orthopyroxene, clinopyroxene, and amphibole, and they were calibrated using major element and REE data of amphibole and pyroxenes in natural mantle samples from intraplate settings. The mineral-melt REE partitioning models suggest that amphibole is not in equilibrium with coexisting pyroxenes in the mantle samples and that the amphibole crystallized at a lower temperature than that of the pyroxenes. We estimated the apparent amphibole crystallization temperature using major element compositions of the amphibole and established temperature- and composition-dependent models that can be used to predict apparent pyroxene-amphibole REE partition coefficients for amphibole-bearing peridotite and pyroxenite from intraplate lithospheric mantle. Apparent pyroxene-amphibole REE partition coefficients predicted by the models can be used to infer REE contents of amphibole from REE contents of coexisting pyroxenes. This is especially useful when the grain size of amphibole is too small for trace element analysis.

Keywords: Amphibole, clinopyroxene, orthopyroxene, peridotite, pyroxenite, REE partitioning, temperature, mineral composition

INTRODUCTION

The lithospheric mantle is composed mainly of nominally anhydrous minerals, including olivine, orthopyroxene, clinopyroxene, spinel, and garnet. Hydrous minerals, such as amphibole and phlogopite, are also present in regions that have been affected by modal metasomatism. Amphibole can be formed by the interaction between peridotite and hydrous melts (e.g., Sen and Dunn 1995; Rapp et al. 1999; Wang et al. 2021) and is stable in the lithospheric mantle at temperatures and pressures up to 1150 °C and 3.8 GPa (e.g., Green 1973; Wallace and Green 1991; Niida and Green 1999; Fumagalli et al. 2009; Mandler and Grove 2016). Under these conditions, particularly within the spinel stability field, amphibole and pyroxene are the main reservoirs of incompatible elements. The trace element contents of pyroxene and amphibole have been used to infer geochemical and petrologic processes that occur in the lithospheric mantle. However, amphibole typically occurs as interstitial grains in mantle rocks. Their small sizes often make trace element analysis challenging, and consequently, concentrations of trace elements in amphibole have not been frequently reported alongside those of coexisting pyroxenes (e.g., Liu et al. 2010; Matusiak-Malek et al. 2017; Aradi et al. 2020; Zhang et al. 2022). The objective of the present study is to provide an interim solution to this problem by developing semi-empirical models for

the distribution of rare earth elements (REEs) between amphibole and pyroxenes.

In general, the partitioning of trace elements between a mineral and its coexisting melt depends on pressure, temperature, and mineral and melt composition. The effects of mineral and melt compositions on REE partitioning between pyroxene and melt and between amphibole and melt have been studied using data from laboratory partitioning experiments and the lattice strain model (e.g., Klein et al. 1997, 2000; Gaetani et al. 2003; Adam and Green 2003, 2006; Gaetani 2004; Sun and Liang 2012, 2013; Yao et al. 2012; Shimizu et al. 2017). The effects of temperature and mineral composition on REE partitioning between orthopyroxene and clinopyroxene have also been investigated using the lattice strain model (e.g., Stosch 1982; Hellebrand et al. 2005; Witt-Eickschen and O'Neill 2005; Lee et al. 2007; Witt-Eickschen et al. 2009; Yao et al. 2012; Liang et al. 2013; Sun and Liang 2014). Yao et al. (2012), Liang et al. (2013), and Sun and Liang (2014) constructed an orthopyroxene-clinopyroxene REE partitioning model from the pyroxene-melt REE partitioning models. Their model suggested that REE partitioning between the two pyroxenes is sensitive to temperature and pyroxene composition and can be used as a thermometer. For two pyroxene-bearing rocks that experienced cooling, the temperatures derived from the REE-in-two-pyroxene thermometer (Liang et al. 2013) are generally higher than temperatures derived from Ca-Mg-Fe based two-pyroxene thermometers (Wells 1977; Brey and Köhler 1990; Putirka 2008) because REEs diffuse more slowly than major elements in pyroxene (Van Orman

* Corresponding author E-mail: c_wang@jlu.edu.cn. Orcid https://orcid.org/0000-0002-8297-1243

et al. 2001, 2002; Dimanov and Wiedenbeck 2006; Cherniak and Liang 2007; Müller et al. 2013).

Amphibole has more structural sites and a larger range of chemical compositions than pyroxene (e.g., Leake et al. 1997; Hawthorne et al. 2012). The composition of amphibole varies with physical conditions and compositions of the metasomatic melt and peridotite in the lithospheric mantle (e.g., Niida and Green 1999; Coltorti et al. 2007; Mandler and Grove 2016; Wang et al. 2021). Variations in the physical conditions and chemical compositions lead to the difference in compositions between amphibole from the supra-subduction zone [S-amphibole of Coltorti et al. (2007)] lithospheric mantle and amphibole from the intraplate [I-amphibole of Coltorti et al. (2007)] lithospheric mantle. In general, the S-amphibole has a higher Mg# [100 × Mg/(Mg + Fe), atomic ratio] and lower Ti, Na, and K contents than the I-amphibole (Coltorti et al. 2007) (Fig. 1). According to the lattice strain model of Shimizu et al. (2017), amphibole-melt REE partition coefficients increase with increasing Ti and decreasing Na, K, and Mg contents of amphibole.

REE partitioning between pyroxene and amphibole likely depends on physical conditions and mineral compositions. Klein et al. (1997) compared the parameters of the lattice strain model for clinopyroxene-melt REE partitioning with those for amphibole-melt REE partitioning. They concluded that similarities in Young's moduli between the M4 site in amphibole and the M2 site in clinopyroxene result in nearly identical clinopyroxene and amphibole REE partition coefficients at given physical conditions, and thus subparallel clinopyroxene and amphibole REE patterns. By comparing the REE contents of coexisting clinopyroxenes and amphiboles in mantle xenoliths from West Eifel, Germany, Witt-Eickschen and Harte (1994) and Witt-Eickschen and O'Neill (2005) inferred that clinopyroxene-amphibole REE partition coefficients are controlled by REE ionic radius and Na content of the clinopyroxene.

Although significant progress has been made in quantifying REE partitioning in amphibole, there is no predictive model for pyroxene-amphibole REE partition coefficients. In this study, we develop temperature- and mineral composition-dependent models for REE partitioning between clinopyroxene, orthopyroxene, and amphibole in mantle rocks. These semi-empirical models are based on lattice strain models of REE partitioning between pyroxene, amphibole, and silicate melt (Sun and Liang 2012, 2013; Yao et al. 2012; Shimizu et al. 2017) and are calibrated using natural amphibole-bearing mantle xenoliths. Because amphibole generally crystallized later than pyroxene in the lithospheric mantle, REE partition coefficients obtained from the semi-empirical models are apparent partition coefficients. Nonetheless, the apparent pyroxene-amphibole REE partition coefficients obtained from our models are useful for estimating the REE concentrations of amphibole from the REE contents of pyroxene, especially when the grain size of amphibole is too small for trace element analysis.

THEORETICAL BASIS

Parameterized mineral-melt REE partitioning models

The theoretical basis of this study is the lattice strain model for partitioning of a REE i between a mineral and its coexisting melt (Brice 1975; Blundy and Wood 1994; Wood and Blundy 1997, 2003), which can be written as:

$$D_i^{\text{min-melt}} = D_0 \exp \left\{ -\frac{4\pi EN_A}{RT} \left[\frac{r_0}{2} (r_0 - r_i)^2 - \frac{1}{3} (r_0 - r_i)^3 \right] \right\} \quad (1)$$

where D_0 is the partition coefficient for strain-free substitution; r_0 is the optimum radius for the lattice site; E is the apparent Young's modulus for the lattice site; r_i is the ionic radius of the REE; T is the temperature in K; R is the gas constant; and N_A is Avogadro constant. In general, the lattice parameters D_0 , r_0 , and E depend on temperature, pressure, and mineral and melt compositions.

Parameterized lattice strain models for amphibole-melt, orthopyroxene-melt, and clinopyroxene-melt REE partitioning were developed by Shimizu et al. (2017), Yao et al. (2012), and Sun and Liang (2012), respectively. These models show that mineral-melt REE partition coefficients depend on temperature and mineral chemistry. With decreasing temperature, mineral-melt REE partition coefficients increase. In the amphibole model of Shimizu et al. (2017), D_0 is positively correlated with Ti in amphibole but negatively correlated with Mg, Na, and K in amphibole, r_0 is negatively correlated with the ferromagnesian content of the M4 site in amphibole ($X_{\text{Fe}}^{\text{M4}}$), and E is a constant. In the low-Ca pyroxene model of Yao et al. (2012), D_0 is positively correlated with Ca content of the M2 site ($X_{\text{Ca}}^{\text{M2}}$) and Al content of the tetrahedral site (X_{Al}^{T}) in the pyroxene, and in the clinopyroxene model of Sun and Liang (2012), D_0 is positively correlated with X_{Al}^{C} and Mg content of the M2 site ($X_{\text{Mg}}^{\text{M2}}$) in the pyroxene. The values of r_0 and E in the two pyroxene models also depend on pyroxene composition. The lattice strain parameters of the three mineral-melt REE partitioning models are summarized in Online Materials¹ Appendix A.

The amphiboles used to calibrate the partitioning model of Shimizu et al. (2017) were produced at 780–1100 °C and 0.2–2.5 GPa through laboratory experiments. Oxygen fugacities of these experiments are –2 to +3.2 logarithmic units from the quartz-fayalite-magnetite buffer, which covers a large range of oxygen fugacities calculated for spinel peridotite from different tectonic settings (Frost and McCammon 2008). The experimental amphiboles contain 0.73–6.35 wt% TiO₂, 1.20–4.04 wt% Na₂O, and 0.03–2.77 wt% K₂O, and have Mg#s ranging from 36 to 100 (Fig. 1). Their compositions overlap with a majority (81%) of I-amphiboles but only a small portion (15%) of S-amphiboles from mantle rocks reported in the literature. The latter has lower TiO₂ and Na₂O but higher SiO₂ and Mg# than amphiboles from the partitioning experiments (Figs. 1a–1c). The Mg#s of clinopyroxenes and low-Ca pyroxenes from the partitioning experiments for calibrating the parameterized models of Sun and Liang (2012, 2013) and Yao et al. (2012) are 54–100 and 70–100, respectively, covering the main range of pyroxene compositions in mantle rocks.

Pyroxene-amphibole REE partitioning models

When two minerals (α and β) and the melt are in thermodynamic equilibrium, it is possible to calculate the mineral–mineral REE partition coefficients by taking the ratio of the two mineral–melt partition coefficients, viz.,

$$D_i^{\beta-\alpha} = \frac{D_i^{\beta-\text{melt}}}{D_i^{\alpha-\text{melt}}} = \frac{D_0^{\beta}}{D_0^{\alpha}} \exp \left\{ -\frac{4\pi E^{\beta} N_A}{RT} \left[\frac{r_0^{\beta}}{2} (r_0^{\beta} - r_i)^2 - \frac{1}{3} (r_0^{\beta} - r_i)^3 \right] + \frac{4\pi E^{\alpha} N_A}{RT} \left[\frac{r_0^{\alpha}}{2} (r_0^{\alpha} - r_i)^2 - \frac{1}{3} (r_0^{\alpha} - r_i)^3 \right] \right\} \quad (2)$$

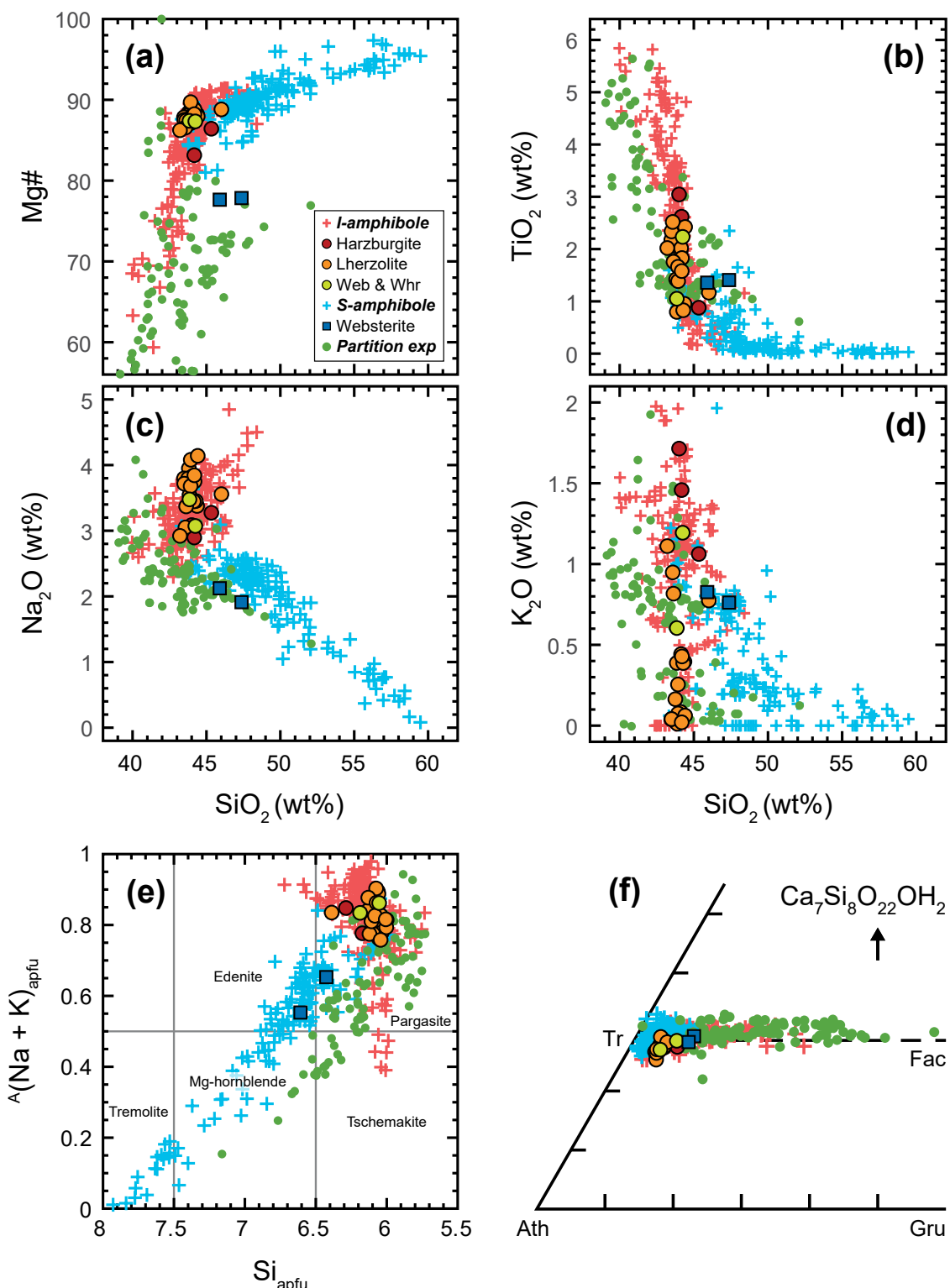


FIGURE 1. Compositions of amphiboles (oxides in wt%, on volatile-free basis) from amphibole-bearing mantle rocks. Red and blue plus signs are intraplate (I)-amphiboles and supra-subduction (S)-amphiboles, respectively, classified after Coltorti et al. (2007). Green dots are amphiboles from the amphibole-melt REE partitioning experiments used to calibrate the model of Shimizu et al. (2017). Closed symbols are amphiboles in mantle samples that have compositions within the range of those used for calibration. The calculation of chemical formulas and the compositional boundaries in e follow those of Leake et al. (1997). Tr = tremolite; Ath = anthophyllite; Fac = ferro-actinolite; Gru = grunerite. (Color online.)

Yao et al. (2012), Liang et al. (2013), and Sun and Liang (2014) demonstrated that Equation 2 reproduces the measured orthopyroxene-clinopyroxene REE partition coefficients in well-equilibrated peridotites and can be used under magmatic and subsolidus conditions. The REE-in-two-pyroxene thermometer of Liang et al. (2013) was developed by rearranging Equation 2. Temperatures obtained from the REE thermometer (T_{REE}) for well-equilibrated peridotites are similar to those obtained from major element-based pyroxene thermometers such as those of Wells (1977), Brey and Köhler (1990), and Putirka (2008) (gray fields in Fig. 2).

Applying Equation 2 to the mineral pairs of pyroxene and amphibole, we have the orthopyroxene-amphibole and clinopyroxene-amphibole REE partitioning models:

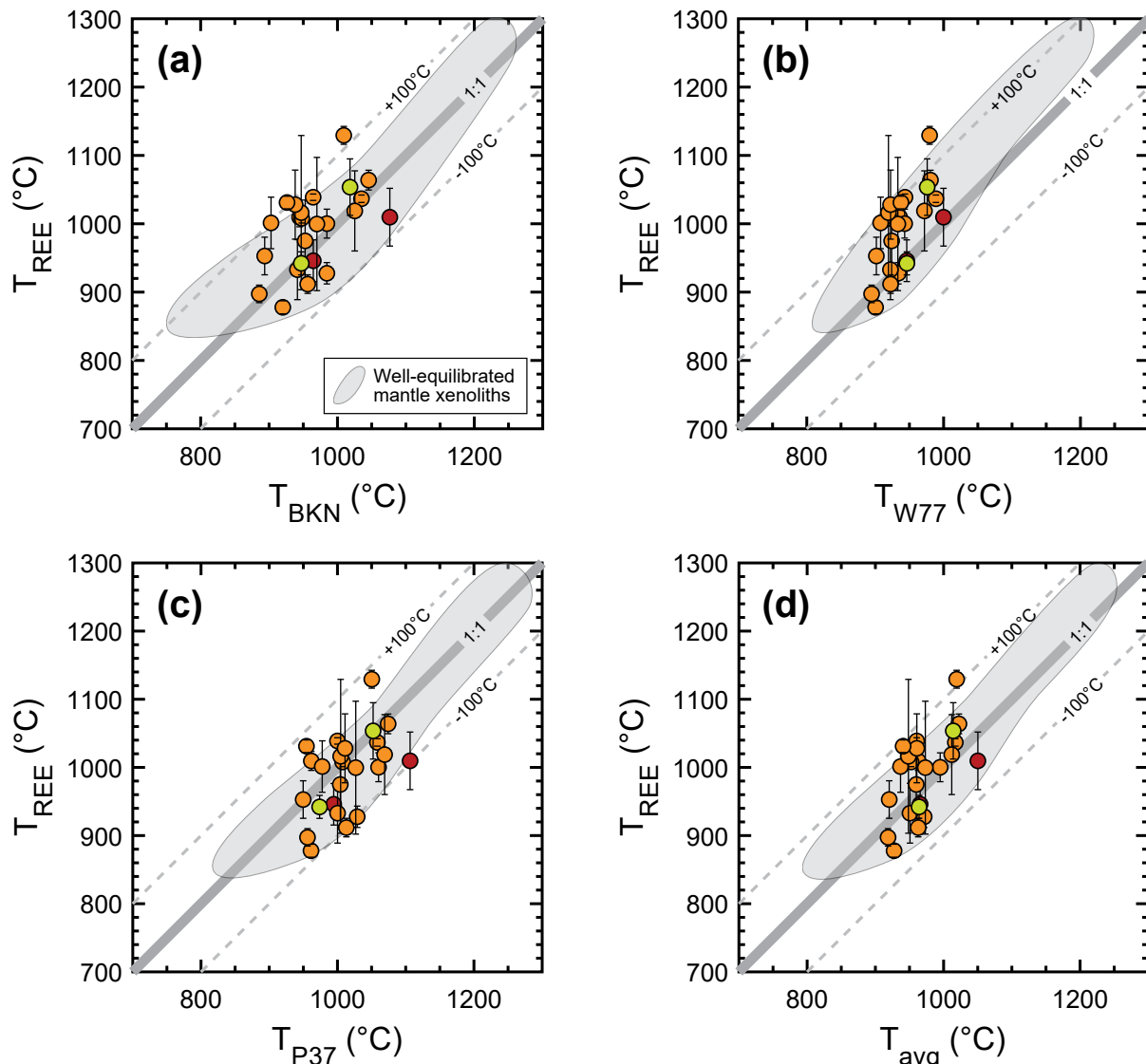


FIGURE 2. Correlations of temperature derived from the REE-in-two-pyroxene thermometer of Liang et al. (2013) (T_{REE}) with those from the major element-based two-pyroxene thermometers of Brey and Köhler (1990) (T_{BKN}), Wells (1977) (T_{W77}), Putirka (2008) (his Eq. 37, T_{P37}), and average of the three (T_{avg}) for the amphibole-bearing mantle rocks. Symbols are the same as in Figure 1. Error bars are 1σ uncertainties in T_{REE} . The solid gray lines denote the 1:1 correlation, and the dashed gray lines denote the ± 100 °C deviations. Gray fields show the ranges of temperatures of well-equilibrated peridotite xenoliths from Liang et al. (2013). (Color online.)

$$D_i^{\text{Pyx-Amp}} = \frac{D_i^{\text{Pyx-melt}}}{D_i^{\text{Amp-melt}}} = \frac{D_0^{\text{Pyx}}}{D_0^{\text{Amp}}} \exp \left\{ \frac{-4\pi E^{\text{Pyx}} N_A}{RT} \left[\frac{r_0^{\text{Pyx}}}{2} (r_0^{\text{Pyx}} - r_i)^2 - \frac{1}{3} (r_0^{\text{Pyx}} - r_i)^3 \right] \right\} \\ + \frac{4\pi E^{\text{Amp}} N_A}{RT} \left[\frac{r_0^{\text{Amp}}}{2} (r_0^{\text{Amp}} - r_i)^2 - \frac{1}{3} (r_0^{\text{Amp}} - r_i)^3 \right] \right\} \quad (3)$$

where Pyx is either orthopyroxene (Opx) or clinopyroxene (Cpx), and the lattice strain parameters are presented in Online Materials¹ Appendix A. Equation 3 is valid so long as pyroxene and amphibole are in chemical equilibrium.

Major element and REE data of pyroxenes and amphibole in amphibole-bearing mantle rocks from the literature can be used

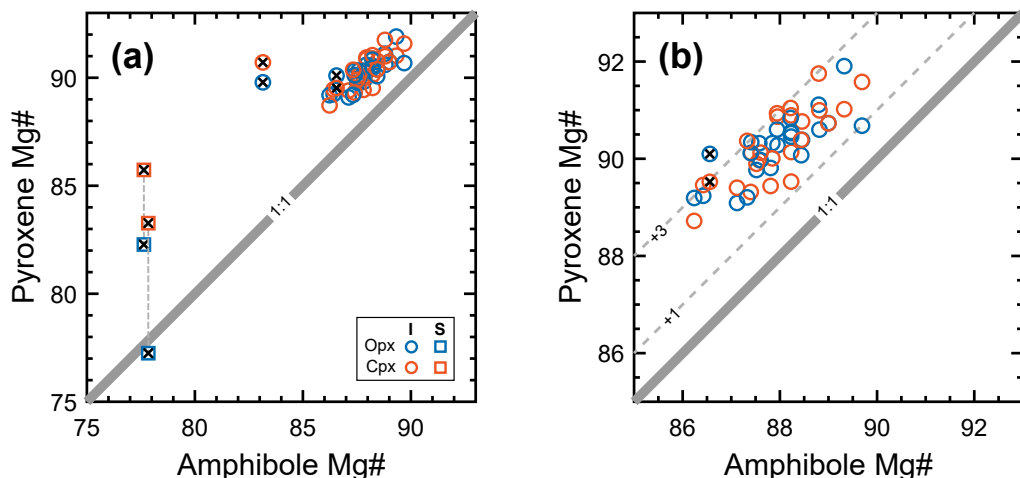


FIGURE 3. Comparisons of amphibole Mg# with orthopyroxene and clinopyroxene Mg#s for the amphibole-bearing mantle samples. Symbols with a cross denote samples that display obvious textual and compositional disequilibrium. See text for details. (Color online.)

to test pyroxene–amphibole REE partitioning models (e.g., Witt-Eickschen and Harte 1994; Grégoire et al. 2000; Witt-Eickschen and O’Neill 2005; Ishimaru et al. 2007; Xu et al. 2010; Bénard and Ionov 2013, 2021; Zhou 2014; Pintér et al. 2015; Matusiak-Małek et al. 2017; Aradi et al. 2020; Belousov et al. 2021; Nishio et al. 2022). To apply these models, a mantle sample must meet the following two requirements: (1) amphibole and pyroxene compositions are within the calibration ranges of the mineral–melt partitioning models, and (2) amphibole and pyroxenes crystallized from the same melt, i.e., formed from the same metasomatic event. The calibration ranges of pyroxene–melt partitioning models of Sun and Liang (2012, 2013) and Yao et al. (2012) cover pyroxene compositions of mantle rocks, including the amphibole-bearing samples in this study. Twenty-eight of the amphibole-bearing mantle rocks from the literature cited above have amphibole compositions within the calibration range of amphibole–melt partitioning model of Shimizu et al. (2017). They include 26 samples with I-amphibole from Western Pannonic Basin, Hungary (Aradi et al. 2020), Nyos Lakes, Cameroon (Pintér et al. 2015), Wilcza Góra, Southwestern Poland (Matusiak-Małek et al. 2017), Huadian, northeastern China (Xu, unpublished), and two samples with S-amphibole from Laiwu, North China Craton (Zhou 2014).

To check if requirement 2 is met, we examined the texture and mineral chemistry for the 28 samples (see Text S1 of Online Materials¹ Appendix C for details.) Among these samples, two peridotites with I-amphibole from Western Pannonic Basin and the two websterites with S-amphibole from Laiwu show significant disequilibrium textures. Additionally, their constituent pyroxenes have significantly higher Mg#s (by 3.5–8.1 units) than amphibole Mg#s (Fig. 3a; Online Materials¹ Table S1). These samples were excluded from the test. The remaining 24 samples all contain I-amphibole. Their orthopyroxene Mg#s are similar to the clinopyroxene Mg#s, but both pyroxene Mg#s are slightly higher (by 1.0–3.0 units) than amphibole Mg# (Fig. 3b; Online Materials¹ Table S1). Figure 2 compares the temperatures calculated using the REE-in-two-pyroxene thermometer (T_{REE} , Liang et al. 2013)

with those calculated using the major-element-based two-pyroxene thermometers of Wells (1977, T_{W77}), Brey and Köhler (1990, T_{BKN}), and Putirka (2008, his Equation 37, T_{P37}), and an average of the three temperatures (T_{avg}) for the 24 amphibole-bearing mantle rocks. Temperatures of these samples are mostly within the range of well-equilibrated mantle xenoliths, suggesting that the REEs (at least the heavy REEs) and major elements in orthopyroxene are in equilibrium with those in clinopyroxene (Liang et al. 2013).

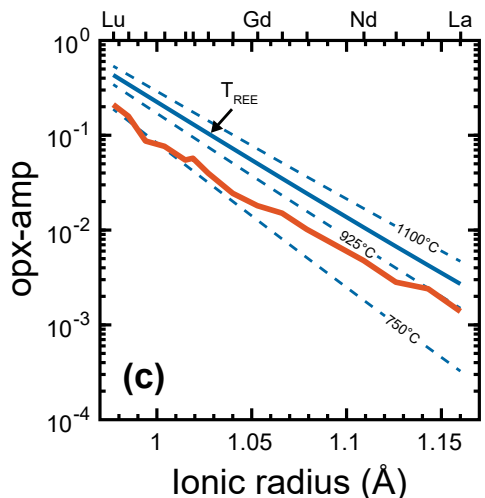
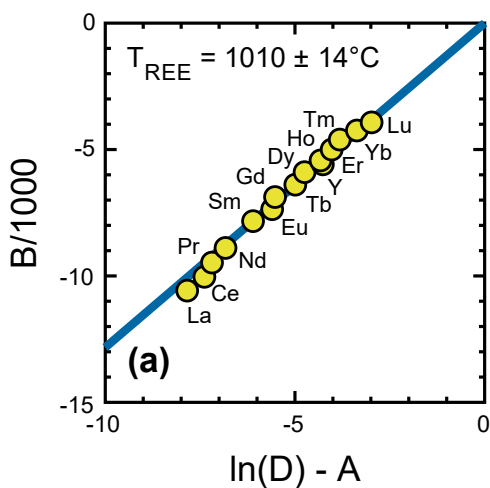
Figure 4a shows the inversion diagram based on the REE-in-two-pyroxene thermometer of Liang et al. (2013) for an amphibole-bearing lherzolite from Wilcza Góra, SW Poland [Matusiak-Małek et al. (2017), sample WLK30]. Using the inverted temperature ($T_{\text{REE}} = 1010 \pm 14$ °C), the mineral–mineral REE partitioning model of Equation 2 well-reproduced orthopyroxene–clinopyroxene partition coefficients for most of the REEs (Fig. 4b). The exceptions are La and Ce, which may be attributed to their higher closure temperatures (Liang 2015).

Interestingly, the pyroxene–amphibole REE partition coefficients calculated using Equation 3, T_{REE} , and major element compositions of the amphibole and pyroxenes differ markedly from the measured values (Figs. 4c and 4d). The isotherms established by the orthopyroxene–amphibole REE partitioning model indicate that orthopyroxene and amphibole would be equilibrated at a lower temperature (between 750 and 925 °C, Fig. 4c). In addition, the model-derived clinopyroxene–amphibole REE partition coefficients are well above the measured values, suggesting REEs in amphibole and clinopyroxene are not in equilibrium at any temperature (Fig. 4d). A likely explanation is that amphibole crystallized at a temperature lower than T_{REE} and that chemical equilibrium between amphibole and the pyroxenes was not established. This is consistent with the observation from hydrous melt–peridotite reactive crystallization experiments of Wang et al. (2021), where the interstitial and overgrowth occurrences of amphibole in the product peridotite and pyroxenite suggest a later crystallization of amphibole than pyroxenes. Below, we present a semi-empirical model that can be used to estimate the crystallization temperature of amphibole in mantle rocks.

Semi-empirical models for crystallization temperature of amphibole

Since the amphibole crystallizes later than the pyroxenes, the pyroxene–melt and amphibole–melt REE partition coefficients are defined at their crystallization temperatures (T^{Pyx} and T^{Amp} , respectively). Taking the ratio of $D^{\text{Pyx-melt}}$ at T^{Pyx} and $D^{\text{Amp-melt}}$ at T^{Amp} , we have, from the lattice strain model (Eq. 1), the pyroxene–amphibole apparent partition coefficient:

$$D_i^{\text{Pyx-Amp}} = \frac{C_i^{\text{Pyx}}}{C_i^{\text{Amp}}} = \frac{D_i^{\text{Pyx-melt}_{\text{Pyx}}} C_i^{\text{melt}_{\text{Pyx}}}}{D_i^{\text{Amp-melt}_{\text{Amp}}} C_i^{\text{melt}_{\text{Amp}}}} = \\ \frac{D_0^{\text{Pyx}} \exp \left\{ -\frac{4\pi E^{\text{Pyx}} N_A}{RT^{\text{Pyx}}} \left[\frac{r_0^{\text{Pyx}}}{2} (r_0^{\text{Pyx}} - r_i)^2 - \frac{1}{3} (r_0^{\text{Pyx}} - r_i)^3 \right] \right\} + \ln \frac{C_i^{\text{melt}_{\text{Pyx}}}}{C_i^{\text{melt}_{\text{Amp}}}}}{D_0^{\text{Amp}} \exp \left\{ +\frac{4\pi E^{\text{Amp}} N_A}{RT^{\text{Amp}}} \left[\frac{r_0^{\text{Amp}}}{2} (r_0^{\text{Amp}} - r_i)^2 - \frac{1}{3} (r_0^{\text{Amp}} - r_i)^3 \right] \right\}} \quad (4)$$



where melt_{Pyx} and melt_{Amp} are melts in equilibrium with pyroxene and amphibole, respectively, and $C_i^{\text{melt}_{\text{Pyx}}} / C_i^{\text{melt}_{\text{Amp}}}$ is the ratio of melt REE concentrations at the two equilibrium temperatures. Given the generally small amount of amphibole crystallized after pyroxenes in the mantle samples and the moderate incompatibility of REEs in amphibole (partition coefficients mostly 0.1–1) at a range of temperatures (780–1100 °C) (Shimizu et al. 2017), we infer that the ratio $C_i^{\text{melt}_{\text{Pyx}}} / C_i^{\text{melt}_{\text{Amp}}}$ is on the order of one, and thus $\ln(C_i^{\text{melt}_{\text{Pyx}}} / C_i^{\text{melt}_{\text{Amp}}})$ is negligible compared to contributions from lattice strains in pyroxenes and amphibole. Hence, Equation 4 can be simplified as:

$$D_i^{\text{Pyx-Amp}} = \frac{D_0^{\text{Pyx}}}{D_0^{\text{Amp}}} \exp \left\{ -\frac{4\pi E^{\text{Pyx}} N_A}{RT^{\text{Pyx}}} \left[\frac{r_0^{\text{Pyx}}}{2} (r_0^{\text{Pyx}} - r_i)^2 - \frac{1}{3} (r_0^{\text{Pyx}} - r_i)^3 \right] \right\} + \frac{4\pi E^{\text{Amp}} N_A}{RT^{\text{Amp}}} \left[\frac{r_0^{\text{Amp}}}{2} (r_0^{\text{Amp}} - r_i)^2 - \frac{1}{3} (r_0^{\text{Amp}} - r_i)^3 \right] \quad (5)$$

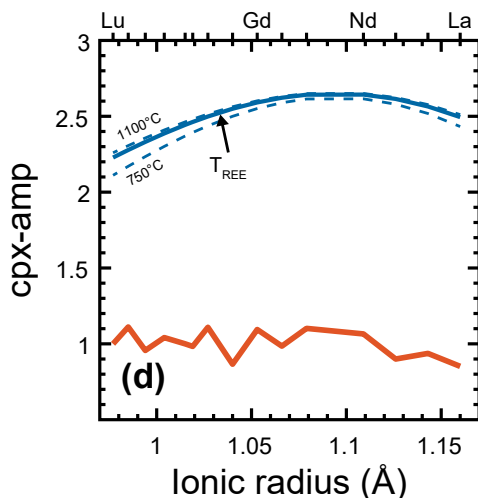
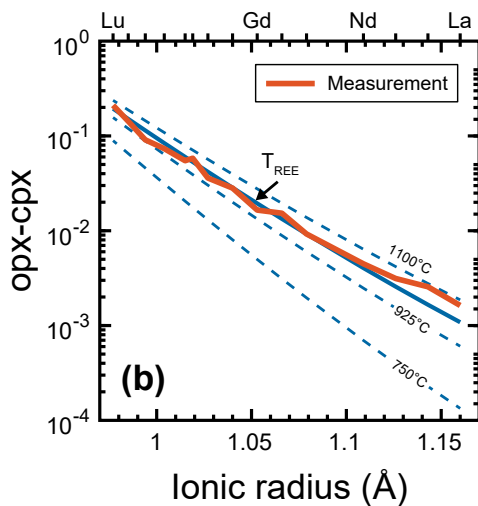


FIGURE 4. (a) Inversion diagram for the REE-in-two-pyroxene temperature (T_{REE}) of an amphibole-bearing lherzolite [sample WLK30 from Wilcza Góra, SW Poland (Matusiak-Malek et al. 2017)]. (b–d) Comparisons of the measured orthopyroxene–clinopyroxene and pyroxene–amphibole REE partition coefficients (solid red patterns) with those calculated using the mineral–mineral REE partitioning model of Equation 2 at the inverted T_{REE} (solid blue curves). Partition coefficients calculated at 750, 925, and 1100 °C are also shown for comparison (dashed blue isotherms). The partition coefficients are plotted against eightfold ionic radii of REEs from Shannon (1976). (Color online.)

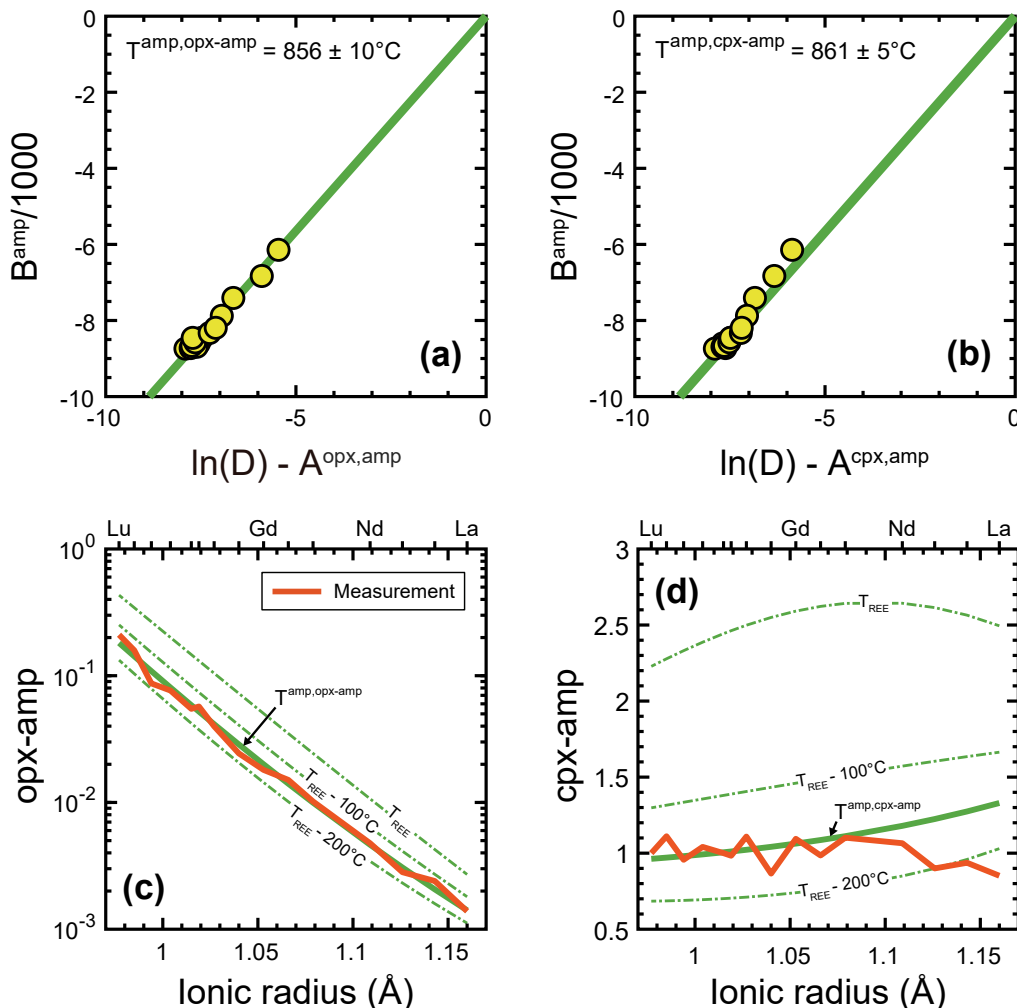


FIGURE 5. (a and b) Inversion diagrams for the apparent amphibole temperatures ($T^{\text{Amp,oxp-amp}}$ and $T^{\text{Amp,cpx-amp}}$) of sample WLK30 (the lherzolite sample shown in Fig. 4) using our semi-empirical models. (c and d) Comparisons of the measured pyroxene-amphibole REE partition coefficients (solid red patterns) with those calculated using the REE partitioning models of Equation 5 with amphibole temperature at the inverted $T^{\text{Amp,oxp-amp}}$ or $T^{\text{Amp,cpx-amp}}$ (solid green curves). Partition coefficients calculated assuming the amphibole temperature at T_{REE} , $T_{\text{REE}} = 100$ °C, and $T_{\text{REE}} = 200$ °C are plotted for comparison (dot-dashed green isotherms). The partition coefficients are plotted against eightfold ionic radii of REEs from Shannon (1976). (Color online.)

where T^{Amp} is the apparent amphibole–melt REE partitioning temperature or amphibole crystallization temperature while neglecting the difference in melt REE concentration [$\ln(C_i^{\text{melt,Pyx}}/C_i^{\text{melt,Amp}})$ in Eq. 4]. Rearranging Equation 5, we have:

$$\ln D_i^{\text{Pyx-Amp}} = A_i^{\text{Pyx,Amp}} + (B_i^{\text{Amp}}/T^{\text{Amp}}). \quad (6)$$

The terms $A_i^{\text{Pyx,Amp}}$ and B_i^{Amp} are presented in Online Materials¹ Appendix B. Equation 6 can be written in the linear form:

$$B_i^{\text{Amp}} = T^{\text{Amp}} (\ln D_i^{\text{Pyx-Amp}} - A_i^{\text{Pyx,Amp}}). \quad (7)$$

In the absence of additional information, we can approximate T^{Pyx} using the temperature derived from the REE-in-two-pyroxene thermometer of Liang et al. (2013) (T_{REE}). The apparent amphibole temperature can be calculated using an inversion diagram constructed by plotting $(\ln D_i^{\text{Opx-Amp}} - A_i^{\text{Opx,Amp}})$ or $(\ln D_i^{\text{Cpx-Amp}} - A_i^{\text{Cpx,Amp}})$ against B_i^{Amp} . The slope of regression line passing through the

origin in the diagram is the apparent temperature.

Figures 5a and 5b display the inversion diagrams of the apparent amphibole temperatures for the amphibole-bearing lherzolite shown in Figure 4 [sample WLK30 from Matusiak-Malek et al. (2017)]. Using a robust linear least-squares regression method, we fit a line through the origin and data in the diagram and obtain the temperature from the slope of this line. Similar apparent temperatures are obtained from the orthopyroxene-amphibole REE partitioning data ($T^{\text{Amp,oxp-amp}} = 856 \pm 10$ °C) and the clinopyroxene-amphibole REE partitioning data ($T^{\text{Amp,cpx-amp}} = 861 \pm 5$ °C). In Figures S1–S24 of Online Materials¹ Appendix C, we present the T^{Amp} inversion diagrams for the 24 mantle samples included in this study. For most of the samples, data of light and some middle REEs are off the regression line, and these outliers were excluded from the inversion. Most of these elements are also outliers in the inversion diagrams when applying the REE-in-two-pyroxene thermometer of Liang et al. (2013). This is attributed in part to the low

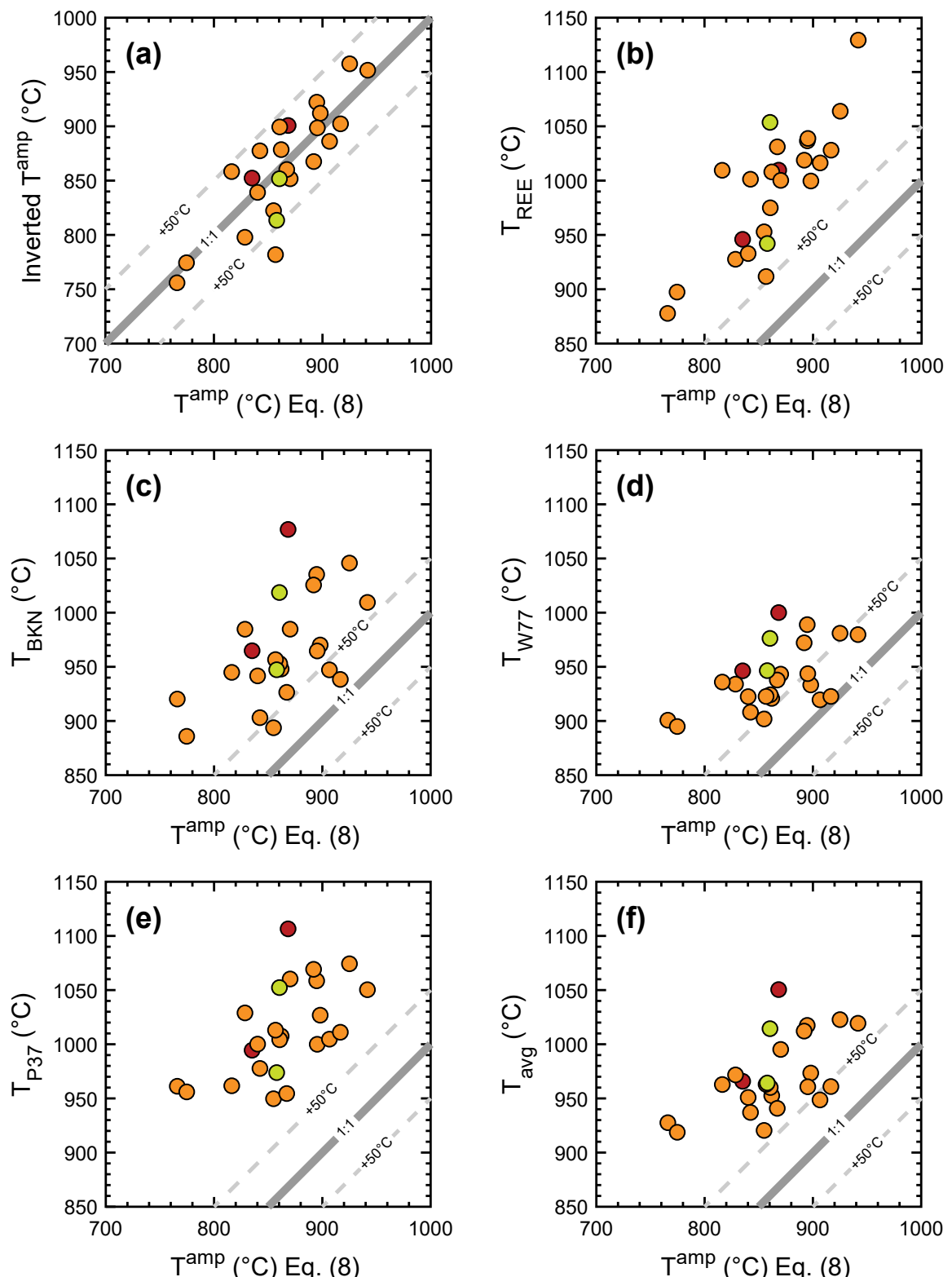


FIGURE 6. Comparisons of the T^{Amp} calculated using Equation 8 with (a) the inverted T^{Amp} (average value of $T^{\text{Amp,Opx-Amp}}$ and $T^{\text{Amp,Cpx-Amp}}$), (b) T_{REE} , and (c–f) major-element derived temperatures for the amphibole-bearing mantle rocks. Symbols are the same as in Figure 1, and the element-based two-pyroxene thermometers are identical to those in Figure 2. The solid gray lines denote the 1:1 correlation, and the dashed gray lines denote the ± 50 °C deviations. (Color online.)

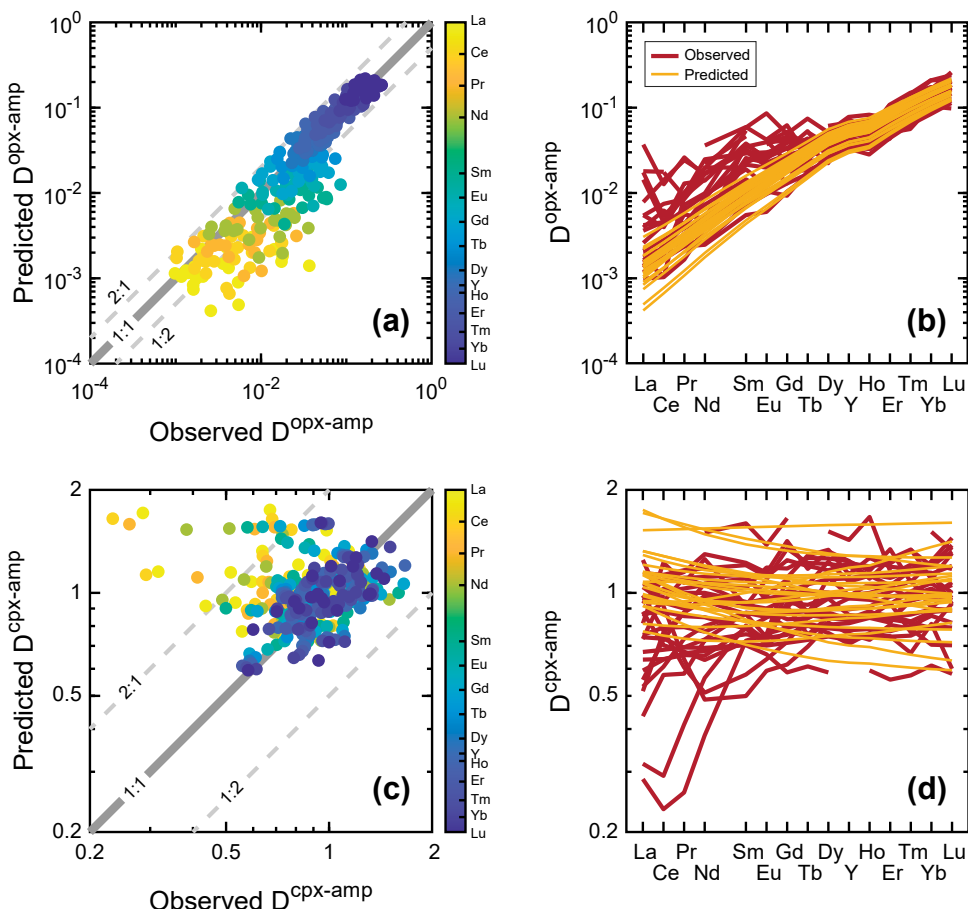


FIGURE 7. Comparison between the measured pyroxene-amphibole REE partition coefficients with those predicted using the partitioning models of Equation 5 and T^{Amp} calculated using Equation 8. The solid gray lines in **a** and **c** denote the 1:1 correlation, and the dashed gray lines denote the 1:2 and 2:1 correlations. Data in **a** and **c** are color-coded with eightfold ionic radii of REEs from Shannon (1976). (Color online.)

analytical precision for the depleted light REEs (Liang et al. 2013) and their higher closure temperatures (Liang 2015). Substituting the inverted amphibole temperature (856 or 861 °C) and T_{REE} (1010 °C) into Equation 5, we obtain orthopyroxene-amphibole and clinopyroxene-amphibole REE partition coefficients. These partition coefficients reproduce the measured values for sample WLK30 (Figs. 5c and 5d). The inverted amphibole temperatures for the amphibole-bearing mantle xenoliths range from 754 °C to 959 °C, which are 69–205 °C lower than T_{REE} values (Online Materials¹ Figs. S1–S24). The amphibole temperatures inverted from the orthopyroxene-amphibole model ($T^{\text{Amp,Opx-Amp}}$) and those from the clinopyroxene-amphibole model ($T^{\text{Amp,Cpx-Amp}}$) are generally in agreement with each other (Online Materials¹ Figs. S1–S24), suggesting the internal consistency of our semi-empirical models.

PARTITION COEFFICIENTS OF REE BETWEEN PYROXENE AND AMPHIBOLE

T-X-dependent pyroxene-amphibole REE partition coefficients

To predict pyroxene-amphibole partition coefficients through temperature (T) and mineral major element composition (X), we

need the amphibole crystallization temperature (T^{Amp}) without relying on its REE data. For this purpose, we fit the inverted T^{Amp} (average value of $T^{\text{Amp,Opx-Amp}}$ and $T^{\text{Amp,Cpx-Amp}}$) with amphibole major element compositions for the 24 samples using the least-squares method, and obtain the empirical expression:

$$T^{\text{Amp}}(\text{°C}) = 258(\pm 33)X_{\text{Si}} + 822(\pm 134)X_{\text{Ti}} - 743(\pm 208)X_{\text{Na}} - 507(\pm 213)X_{\text{K}} + 755(\pm 131)X_{\text{Fe}}^{\text{M4}} - 273.15. \quad (8)$$

The amphibole components are calculated using the method of Shimizu et al. (2017), which is described in Text S2 of Online Materials¹ Appendix C. Numbers in parentheses are the standard error of the coefficients. We also attempted to include pyroxene components in the regression, such as Al, Mg, Ca, and Na. The prediction is not significantly improved, and large uncertainties are introduced. The T^{Amp} calculated using Equation 8 is generally within ± 50 °C deviation from the T^{Amp} inverted using the partitioning models of Equation 7 (Fig. 6a). The calculated T^{Amp} are commonly lower than temperatures calculated from the two-pyroxene thermometers (T_{REE} , T_{BKN} , T_{W77} , and T_{P37} , Figs. 6b–6f). The empirical Equation 8 for T^{Amp} allows us to predict $D^{\text{Opx-Amp}}$ and $D^{\text{Cpx-Amp}}$ for amphibole-bearing mantle samples using Equation 5.

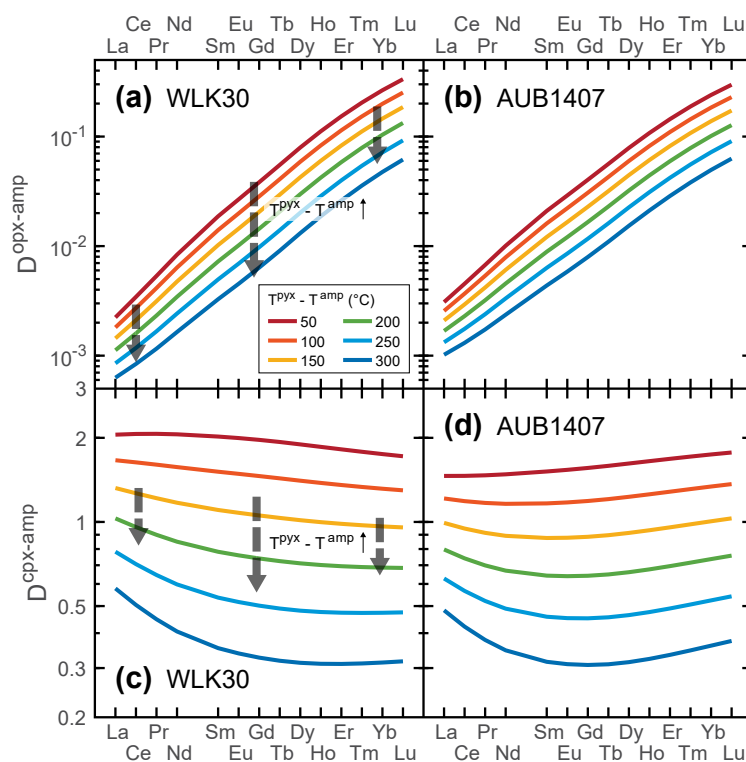


FIGURE 8. Patterns of pyroxene-amphibole REE partition coefficients calculated from the partitioning model of Equation 5 with T^{Amp} assumed to be 50–300 °C lower than the T^{Pyx} (assigned as T_{REE}) for the lherzolites WLK30 from Wilcza Góra (Matusiak-Malek et al. 2017) and AUB1407 from the Western Pannonian Basin, Hungary (Aradi et al. 2020). See text for discussions. (Color online.)

As shown in Figure 8, the calculated pyroxene-amphibole REE partition coefficients decrease systematically with increasing deviation of T^{Amp} from T^{Pyx} . This is attributed to the negative correlation of amphibole–melt REE partition coefficients with temperature (Shimizu et al. 2017). In addition, with increasing deviation of T^{Amp} from T^{Pyx} , the pyroxene–amphibole mid-REE partition coefficients decrease more dramatically than heavy and light REE partition coefficients. Since amphibole generally crystallizes after pyroxenes during hydrous melt–peridotite reactions (e.g., Wang et al. 2021), the preceding exercise underscores the importance of crystallization sequence on the REE distributions between pyroxenes and amphibole.

FIELD APPLICATIONS

Conditions of application and a program for calculation

The semi-empirical partitioning models presented in the preceding sections (Eqs. 5–8) can be used to calculate apparent pyroxene–amphibole REE partition coefficients for amphibole-bearing mantle rocks that have mineral compositions comparable to those from experiments used to calibrate the mineral–melt REE partitioning models (Sun and Liang 2012, 2013; Yao et al. 2012; Shimizu et al. 2017). The pyroxene–melt models cover the main range of pyroxene compositions in mantle rocks, whereas the amphibole–melt model covers mostly the I-amphiboles (Fig. 1). Hence it is important to check amphibole chemistry before an application. Another caveat is that the constituent amphibole and pyroxenes were formed or affected by the same metasomatic event. This can be assessed from texture and mineral composition (e.g., Mg#s). As we have shown in Figure 2b, the amphibole Mg# is slightly lower than the pyroxene Mg#s, and the differences between pyroxene Mg#s and amphibole Mg# in samples for calibration are less than three units.

In the Online Materials¹ Appendix D, we provide an Excel worksheet that can be used to calculate pyroxene–amphibole REE partition coefficients for amphibole-bearing mantle rocks. It requires inputs of pyroxene and amphibole major element compositions and T^{Pyx} . The pyroxene temperature can be estimated using the REE-in-two-pyroxene thermometer of Liang et al. (2013). For mantle rocks from well equilibrated lithospheric mantle, major element-derived temperatures are similar to T_{REE} (Fig. 2). Temperatures calculated using pyroxene thermometers such as T_{BKN} , T_{P37} , and T_{W77} can also be used as T^{Pyx} when T_{REE} is inaccessible.

Applications

To test and validate the pyroxene–amphibole REE partitioning models, we calculate the REE contents of amphibole-bearing

Figure 7 compares the predicted pyroxene–amphibole REE partition coefficients with measured values for the amphibole-bearing mantle rocks. T^{Amp} in the models is calculated using Equation 8. The models are capable of reproducing the partition coefficients of Dy–Lu and Y. The orthopyroxene–amphibole model underestimates some of the La–Tb partition coefficients (Figs. 7a and 7b). Out of 341 orthopyroxene–amphibole REE partition coefficients, 78 (mostly La–Sm) plot below the 1:2 correlation line (Fig. 7a). These outliers are also the outliers on the inversion diagrams for T_{REE} and T^{Amp} (Online Materials¹ Figs. S1–S24). The clinopyroxene–amphibole model does a better job for reproducing REE partition coefficients for the mantle samples than the orthopyroxene–amphibole model (Figs. 7c and 7d). Out of 356 orthopyroxene–amphibole REE partition coefficients, 20 (mostly La–Nd) plot above the 2:1 correlation line, and 94% of the data plot between the 1:2 and 2:1 correlation lines (Fig. 7c).

Effect of amphibole crystallization temperature

We have demonstrated that in the pyroxene–amphibole REE partitioning models the amphibole temperature (T^{Amp}) is generally lower than T^{Pyx} (Fig. 6). To test the effect of amphibole crystallization temperature on pyroxene–amphibole REE partitioning, we calculated pyroxene–amphibole REE partition coefficients for the lherzolite from Wilcza Góra [Matusiak-Malek et al. (2017), sample WLK30] and a lherzolite from the Western Pannonian Basin, Hungary [Aradi et al. (2020), sample AUB1407], using the models presented above and assuming T^{Amp} values that are 50–300 °C lower than T^{Pyx} (assigned as T_{REE}). Although major element compositions and modal mineral abundances vary during cooling, no model is available to account for these changes, and we neglected these variations for the purpose of this exercise.

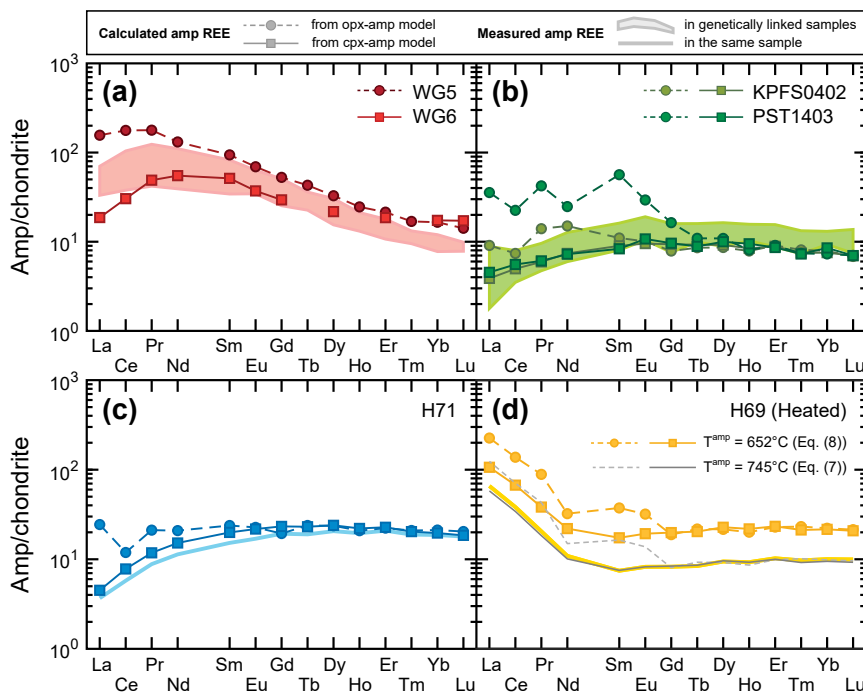


FIGURE 9. Chondrite-normalized REE patterns of amphiboles calculated using the semi-empirical pyroxene-amphibole REE partitioning models and REE contents in the coexisting pyroxenes for amphibole-bearing peridotite xenoliths (a) WG5 and WG6 from Wilcza Góra (Matusiak-Małek et al. 2017), (b) KPFS0402 and PST1403 from Western Pannonian Basin (Aradi et al. 2020), and (c) H71 and (d) H69 from Cameroon volcanic line (Puziewicz et al. 2023). Gray patterns in (d) were calculated using T^{amp} inverted from Equation 7, which testifies the effect of heating. Also plotted for comparison are measured REE patterns of amphiboles in the Wilcza Góra xenoliths genetically related to WG5 and WG6 (Matusiak-Małek et al. 2017), Western Pannonian Basin xenoliths genetically related to KPFS0402 and PST1403 (Aradi et al. 2020), and Cameroon xenoliths H71 and H69 (Puziewicz et al. 2023). The chondrite REE abundances are from Anders and Grevese (1989). (Color online.)

mantle xenoliths and compare them with the measured amphibole REE contents. [Additional tests of the models on peridotite xenoliths from Eifel, western Germany (Witt-Eickschen and Harte 1994; Eickschen and O'Neill 2005) are presented in Online Materials¹ Text S3 of the Online Appendix C.]

The harzburgite xenoliths WG5 and WG6 from Wilcza Góra, Poland (Matusiak-Małek et al. 2017), consist of coarse grains of olivine, orthopyroxene (\pm clinopyroxene), and fine-grained intergranular aggregates. The aggregates contain secondary amphibole and clinopyroxene (\pm phlogopite). Matusiak-Małek et al. (2017) reported major element and REE compositions of the orthopyroxenes for WG5, clinopyroxenes for WG6, and major element compositions of amphiboles for both samples. Mg#s in pyroxene and amphibole are similar (91 in orthopyroxene and 89 in amphibole for WG5, and 88 in clinopyroxene and 85 in amphibole for WG6). They calculated pyroxene temperatures using the Al-in-orthopyroxene thermometer of Witt-Eickschen and Seck (1991) for WG5 (990 °C) and the REE-in-two-pyroxene thermometer of Liang et al. (2013) for WG6 (1023 °C). Using the available data and our models, we obtained T^{amps} for WG5 (888 °C) and WG6 (852 °C), and calculated pyroxene-amphibole REE partition coefficients and REE contents of the amphiboles. The chondrite-normalized REE patterns are presented in Figure 9a. The calculated amphibole REE patterns of samples WG5 and WG6 are similar to those of the genetically related samples (Matusiak-Małek et al. 2017). The predicted REE contents of the amphibole in WG5 are higher than those of the other samples, and the predicted REE pattern for the amphibole in WG6 shows less fractionation between light and heavy REEs than those of the other samples [pink field in Fig. 9a; Matusiak-Małek et al. (2017)]. These are consistent with differences in the REE patterns of the pyroxene in WG5 and WG6, and in the other samples [Figs. 6c and 7e in Matusiak-Małek et al. (2017)].

Another set of examples is the lherzolite xenoliths KPFS0402

and PST1403 from the Western Pannonian Basin, Hungary (Aradi et al. 2020). KPFS0402 has a protogranular texture and contains 0.2% amphibole, and PST1403 has a porphyroclastic texture with 0.02% amphibole. The amphibole crystals in both xenoliths grew on the rims of clinopyroxene and spinel grains. The two samples have uniform orthopyroxene, clinopyroxene, and amphibole Mg#s (90/89/88 and 91/91/89). Using the reported mineral compositional data, we calculated T_{REE} (1025 and 1018 °C) and T^{amp} (927 and 929 °C) for the two samples, as well as the pyroxene-amphibole REE partition coefficients. The REE contents of amphibole in the two samples were calculated using the partition coefficients and the measured clinopyroxene and orthopyroxene REE data are plotted in Figure 9b. The amphibole REE patterns are comparable to measured patterns of amphiboles in xenoliths that have similar petrologic features and sample locations [green field in Fig. 9b; Aradi et al. (2020)]. Amphibole REE patterns calculated from orthopyroxene-amphibole partitioning are perturbed for REEs from La to Gd. This perturbation is in correspondence with those in the orthopyroxene REE patterns (Aradi et al. 2020), which is likely a result of the low concentrations of the light to middle REEs in orthopyroxene relative to the analytical precision.

Recently, Puziewicz et al. (2023) reported two amphibole-bearing lherzolites from the Cameroon volcanic line. Sample H71 has a porphyroclastic texture, and small amphiboles (1%) are dispersed among olivine and pyroxene grains. It has similar T_{REE} (901 °C) and T_{BKN} (911 °C). Orthopyroxene, clinopyroxene, and amphibole have similar Mg#s (90, 92, and 89). Using the reported mineral major element data and T_{REE} , we calculated T^{amp} (778 °C) and pyroxene-amphibole REE partition coefficients. The predicted REE patterns are compared with the measured pattern in Figure 9c. The models mimic middle to heavy REE pattern of the amphibole but slightly overestimate concentrations of light REEs. The elevated La, Ce, and Pr in amphibole follow

that of orthopyroxene REEs.

The other Cameroon lherzolite (sample H69 from Puziewicz et al. 2023) has a sheared texture and contains more abundant amphibole (3.9%). The amphibole forms asymmetric aggregates around spinels and is unevenly distributed in the sample. T_{BKN} (952 °C) of this sample is considerably higher than T_{REE} (872 °C), which suggests a possible heating event after the formation of pyroxenes. T^{Amp} obtained from Equation 8 are 652 °C. Our models overestimate amphibole REE contents, even for the heavy REEs (Fig. 9d). This suggests that Equation 8 is not capable of estimating amphibole temperature from compositions of pyroxene and amphibole that experienced heating. T^{Amp} is likely higher than the calculated values since $D^{\text{Pyx-Amp}}$ s increase with decreasing difference between T^{Pyx} and T^{Amp} (Fig. 8). This can be evidenced by the inverted T^{Amp} using the REE partitioning models of Equation 7. Both the orthopyroxene-amphibole and clinopyroxene-amphibole models yield an T^{Amp} of 745 °C (Fig. 9d).

IMPLICATIONS

The temperature- and composition-dependent REE partitioning models presented in this study make it possible to estimate REE concentrations in amphibole in mantle rocks using REE contents of coexisting orthopyroxene or clinopyroxene. The new partitioning models require major element compositions of amphibole and pyroxenes and the temperature at which the pyroxenes equilibrated. This temperature can be obtained from pyroxene thermometers, including those of Wells (1977), Brey and Köhler (1990), Putirka (2008), and Liang et al. (2013).

The amphibole crystallization temperature has been quantified using thermometers based on amphibole composition, the coexisting melt composition, or a combination of the two (e.g., Ridolfi and Renzulli 2012; Molina et al. 2015; Putirka 2016). However, these thermometers were not designed for mantle rocks. The REE partitioning models (Eq. 7) or the empirical Equation 8 that are calibrated for mantle rocks can be used to invert or calculate amphibole crystallization temperature. Hence, the semi-empirical and empirical models for amphibole crystallization temperature presented in this study have potential implications for constraining the thermal property of the amphibole-bearing lithospheric mantle.

ACKNOWLEDGMENTS AND FUNDING

We thank Federico Casetta and Chun-Ming Wu for their detailed comments and constructive suggestions which helped to improve this manuscript. We also thank Julie Roberge for the editorial handling. This work was supported by grants from National Natural Science Foundation of China (42072072), U.S. National Science Foundation (EAR-2147598), JLU Science and Technology Innovative Research Team (2021TD-05), and European Research Council under the European Union's Horizon 2020 research and innovation program (ERC-Synergy MEET 856555).

REFERENCES CITED

Adam, J. and Green, T. (2003) The influence of pressure, mineral composition and water on trace element partitioning between clinopyroxene, amphibole and basanitic melts. *European Journal of Mineralogy*, 15, 831–841, <https://doi.org/10.1127/0935-1221/2003/0015-0831>.

— (2006) Trace element partitioning between mica- and amphibole-bearing garnet lherzolite and hydrous basanitic melt: 1. Experimental results and the investigation of controls on partitioning behaviour. *Contributions to Mineralogy and Petrology*, 152, 1–17, <https://doi.org/10.1007/s00410-006-0085-4>.

Anders, E. and Grevesse, N. (1989) Abundances of the elements: Meteoritic and solar. *Geochimica et Cosmochimica Acta*, 53, 197–214, [https://doi.org/10.1016/0016-7037\(89\)90286-X](https://doi.org/10.1016/0016-7037(89)90286-X).

Aradi, L.E., Bali, E., Patkó, L., Hidas, K., Kovács, I.J., Zanetti, A., Garrido, C.J., and Szabo, C. (2020) Geochemical evolution of the lithospheric mantle beneath the Styrian Basin (Western Pannonian Basin). *Lithos*, 378–379, 105831, <https://doi.org/10.1016/j.lithos.2020.105831>.

Belousov, I., Batanova, V., Sobolev, A., Savelieva, G., Danyushevsky, L., and Draayers, E. (2021) Pyroxenites from mantle section of Voykar Ophiolite—Melt/peridotite reaction and crystallization in SSZ mantle. *Lithos*, 388–389, 106063, <https://doi.org/10.1016/j.lithos.2021.106063>.

Bénard, A. and Ionov, D.A. (2013) Melt- and fluid-rock interaction in supra-subduction lithospheric mantle: Evidence from andesite-hosted veined peridotite xenoliths. *Journal of Petrology*, 54, 2339–2378, <https://doi.org/10.1093/petrology/egt050>.

Bénard, A., Müntener, O., Pilet, S., Arculus, R.J., and Nebel, O. (2021) Silica-rich spinel harzburgite residues formed by fractional hybridization-melting of the intra-oceanic supra-subduction zone mantle: New evidence from TUBAF seamount peridotites. *Geochimica et Cosmochimica Acta*, 293, 477–506, <https://doi.org/10.1016/j.gca.2020.11.001>.

Blundy, J. and Wood, B. (1994) Prediction of crystal-melt partition coefficients from elastic moduli. *Nature*, 372, 452–454, <https://doi.org/10.1038/372452a0>.

Brey, G.P. and Köhler, T. (1990) Geothermobarometry in four-phase lherzolites II. New thermobarometers, and practical assessment of existing thermobarometers. *Journal of Petrology*, 31, 1353–1378, <https://doi.org/10.1093/petrology/31.6.1353>.

Brice, J.C. (1975) Some thermodynamic aspects of the growth of strained crystals. *Journal of Crystal Growth*, 28, 249–253, [https://doi.org/10.1016/0022-0248\(75\)90241-9](https://doi.org/10.1016/0022-0248(75)90241-9).

Cherniak, D.J. and Liang, Y. (2007) Rare earth element diffusion in natural enstatite. *Geochimica et Cosmochimica Acta*, 71, 1324–1340, <https://doi.org/10.1016/j.gca.2006.12.001>.

Coltorti, M., Bonadiman, C., Faccini, B., Grégoire, M., O'Reilly, S.Y., and Powell, W. (2007) Amphiboles from suprasubduction and intraplate lithospheric mantle. *Lithos*, 99, 68–84, <https://doi.org/10.1016/j.lithos.2007.05.009>.

Dimanov, A. and Wiedenbeck, M. (2006) (Fe, Mg)-Mg interdiffusion in natural diopside: Effect of $p\text{O}_2$. *European Journal of Mineralogy*, 18, 705–718, <https://doi.org/10.1127/0935-1221/2006/0018-0705>.

Frost, D.J. and McCammon, C.A. (2008) The redox state of Earth's mantle. *Annual Review of Earth and Planetary Sciences*, 36, 389–420, <https://doi.org/10.1146/annurev.earth.36.031207.124322>.

Fumagalli, P., Zanchetta, S., and Poli, S. (2009) Alkali in phlogopite and amphibole and their effects on phase relations in metasomatized peridotites: A high-pressure study. *Contributions to Mineralogy and Petrology*, 158, 723–737, <https://doi.org/10.1007/s00410-009-0407-4>.

Gaetani, G.A. (2004) The influence of melt structure on trace element partitioning near the peridotite solidus. *Contributions to Mineralogy and Petrology*, 147, 511–527, <https://doi.org/10.1007/s00410-004-0575-1>.

Gaetani, G.A., Kent, A.J., Grove, T.L., Hutcheon, I.D., and Stolper, E.M. (2003) Mineral/melt partitioning of trace elements during hydrous peridotite partial melting. *Contributions to Mineralogy and Petrology*, 145, 391–405, <https://doi.org/10.1007/s00410-003-0447-0>.

Green, D.H. (1973) Experimental melting studies on a model upper mantle composition at high pressure under water-saturated and water-undersaturated conditions. *Earth and Planetary Science Letters*, 19, 37–53, [https://doi.org/10.1016/0012-821X\(73\)90176-3](https://doi.org/10.1016/0012-821X(73)90176-3).

Grégoire, M., Lorand, J.P., O'Reilly, S.Y., and Cottin, J.Y. (2000) Armalcolite-bearing Ti-rich metasomatic assemblages in harzburgitic xenoliths from the Kerguelen Islands: Implications for the oceanic mantle budget of high-field strength elements. *Geochimica et Cosmochimica Acta*, 64, 673–694, [https://doi.org/10.1016/S0016-7037\(99\)00345-2](https://doi.org/10.1016/S0016-7037(99)00345-2).

Hawthorne, F.C. (1983) The crystal chemistry of the amphiboles. *Canadian Mineralogist*, 2, 173–480.

Hawthorne, F.C., Oberti, R., Harlow, G.E., Maresch, W.V., Martin, R.F., Schumacher, J.C., and Welch, M.D. (2012) Nomenclature of the amphibole supergroup. *American Mineralogist*, 97, 2031–2048, <https://doi.org/10.2138/am.2012.4276>.

Hellebrand, E., Snow, J.E., Mostefaiou, S., and Hoppe, P. (2005) Trace element distribution between orthopyroxene and clinopyroxene in peridotites from the Gakkel Ridge: A SIMS and NanoSIMS study. *Contributions to Mineralogy and Petrology*, 150, 486–504, <https://doi.org/10.1007/s00410-005-0036-5>.

Ishimaru, S., Arai, S., Ishida, Y., Shirasaka, M., and Okrugin, V.M. (2007) Melting and multi-stage metasomatism in the mantle wedge beneath a frontal arc inferred from highly depleted peridotite xenoliths from the Avacha volcano, Southern Kamchatka. *Journal of Petrology*, 48, 395–433, <https://doi.org/10.1093/petrology/egl065>.

Klein, M., Stosch, H.G., and Seck, H.A. (1997) Partitioning of high field-strength and rare-earth elements between amphibole and quartz-dioritic to tonalitic melts: An experimental study. *Chemical Geology*, 138, 257–271, [https://doi.org/10.1016/S0009-2541\(97\)00019-3](https://doi.org/10.1016/S0009-2541(97)00019-3).

Klein, M., Stosch, H.G., Seck, H.A., and Shimizu, N. (2000) Experimental partitioning of high field strength and rare earth elements between clinopyroxene and garnet in andesitic to tonalitic systems. *Geochimica et Cosmochimica Acta*, 64, 99–115, [https://doi.org/10.1016/S0016-7037\(99\)00178-7](https://doi.org/10.1016/S0016-7037(99)00178-7).

Leake, B.E., Woolley, A.R., Arps, C.E.S., Birch, W.D., Gilbert, M.C., Grice, J.D., Hawthorne, F.C., Kato, A., Kisch, H.J., Krivovichev, V.G., and others. (1997) Nomenclature of amphiboles: Report of the subcommittee on amphiboles of the International Mineralogical Association, Commission on New Minerals and Mineral Names. *Canadian Mineralogist*, 35, 219–246.

Lee, C.T.A., Harbert, A., and Leeman, W.P. (2007) Extension of lattice strain theory to mineral/mineral rare-earth element partitioning: An approach for assessing disequilibrium and developing internally consistent partition coefficient between olivine, orthopyroxene, clinopyroxene and basaltic melt. *Geochimica et Cosmochimica Acta*, 71, 481–496, <https://doi.org/10.1016/j.gca.2006.09.014>.

Liang, Y. (2015) A simple model for closure temperature of a trace element in cooling bi-mineralic systems. *Geochimica et Cosmochimica Acta*, 165, 35–43, <https://doi.org/10.1016/j.gca.2015.05.028>.

Liang, Y., Sun, C., and Yao, L. (2013) A REE-in-two-pyroxene thermometer for mafic and ultramafic rocks. *Geochimica et Cosmochimica Acta*, 102, 246–260, <https://doi.org/10.1016/j.gca.2012.10.035>.

Liu, C.Z., Wu, F.Y., Wilde, S.A., Yu, L.J., and Li, J.L. (2010) Anorthitic plagioclase and pargasitic amphibole in mantle peridotites from the Yungbwa ophiolite (southwestern Tibetan Plateau) formed by hydrous melt metasomatism. *Lithos*, 114, 413–422, <https://doi.org/10.1016/j.lithos.2009.10.008>.

Mandler, B.E. and Grove, T.L. (2016) Controls on the stability and composition of amphibole in the Earth's mantle. *Contributions to Mineralogy and Petrology*, 171, 68, <https://doi.org/10.1007/s00410-016-1281-5>.

Matusiak-Malek, M., Puziewicz, J., Ntaflos, T., Grégoire, M., Kukula, A., and Wojtulek, P.M. (2017) Origin and evolution of rare amphibole-bearing mantle peridotites from Wilcza Góra (SW Poland), Central Europe. *Lithos*, 286–287, 302–323, <https://doi.org/10.1016/j.lithos.2017.06.017>.

Molina, J.F., Moreno, J.A., Castro, A., Rodríguez, C., and Fershtater, G.B. (2015) Calcic amphibole thermobarometry in metamorphic and igneous rocks: New calibrations based on plagioclase/amphibole Al-Si partitioning and amphibole-liquid Mg partitioning. *Lithos*, 232, 286–305, <https://doi.org/10.1016/j.lithos.2015.06.027>.

Müller, T., Dohmen, R., Becker, H.W., ter Heege, J.H., and Chakraborty, S. (2013) Fe–Mg interdiffusion rates in clinopyroxene: Experimental data and implications for Fe–Mg exchange geothermometers. *Contributions to Mineralogy and Petrology*, 166, 1563–1576, <https://doi.org/10.1007/s00410-013-0941-y>.

Niida, K. and Green, D.H. (1999) Stability and chemical composition of pargasitic amphibole in MORB pyrolite under upper mantle conditions. *Contributions to Mineralogy and Petrology*, 135, 18–40, <https://doi.org/10.1007/s00410-00050495>.

Nishio, I., Morishita, T., Itano, K., Guotana, J.M., Tamura, A., Szilas, K., Harigane, Y., Tani, K., and Pearson, D.G. (2022) Metasomatic modification of the Mesoarchean Ulamertoq ultramafic body, southern West Greenland. *Journal of Petrology*, 63, egac004, <https://doi.org/10.1093/petrology/egac004>.

Pintér, Z., Patkó, L., Tene Djoukam, J.F., Kovács, I., Tchouankoue, J.P., Falus, G., Konc, Z., Tommasi, A., Barou, F., Mihály, J., and others. (2015) Characterization of the sub-continental lithospheric mantle beneath the Cameron volcanic line inferred from alkaline basalt hosted peridotite xenoliths from Barombi Mbo and Nyos Lakes. *Journal of African Earth Sciences*, 111, 170–193, <https://doi.org/10.1016/j.jafrearsci.2015.07.006>.

Putirka, K.D. (2008) Thermometers and barometers for volcanic systems. *Reviews in Mineralogy and Geochemistry*, 69, 61–120, <https://doi.org/10.2138/rmg.2008.69.3>.

— (2016) Amphibole thermometers and barometers for igneous systems and some implications for eruption mechanisms of felsic magmas at arc volcanoes. *American Mineralogist*, 101, 841–858.

Puziewicz, J., Aulbach, S., Kaczmarek, M.A., Ntaflos, T., Gerdes, A., Mazurek, H., Kukula, A., Matusiak-Malek, M., Tedonkenfack, S.S.T., and Ziobro-Mikrut, M. (2023) The origin and evolution of DMM-like lithospheric mantle beneath continents: Mantle xenoliths from the Oku Volcanic Group in the Cameroon Volcanic Line, West Africa. *Journal of Petrology*, 64, egad049, <https://doi.org/10.1093/petrology/egad049>.

Rapp, R.P., Shimizu, N., Norman, M.D., and Applegate, G.S. (1999) Reaction between slab-derived melts and peridotite in the mantle wedge: Experimental constraints at 3.8 GPa. *Chemical Geology*, 160, 335–356, [https://doi.org/10.1016/S0009-2541\(99\)00106-0](https://doi.org/10.1016/S0009-2541(99)00106-0).

Ridolfi, F. and Renzulli, A. (2012) Calcic amphiboles in calc-alkaline and alkaline magmas: Thermobarometric and chemometric empirical equations valid up to 1,130 °C and 2.2 GPa. *Contributions to Mineralogy and Petrology*, 163, 877–895, <https://doi.org/10.1007/s00410-011-0704-6>.

Sen, C. and Dunn, T. (1995) Experimental modal metasomatism of a spinel lherzolite and the production of amphibole-bearing peridotite. *Contributions to Mineralogy and Petrology*, 119, 422–432, <https://doi.org/10.1007/BF00286939>.

Shannon, R.D. (1976) Revised effective ionic radii and systematic studies of interatomic distances in halides and chalcogenides. *Acta Crystallographica Section A*, 32, 751–767, <https://doi.org/10.1107/S0567739476001551>.

Shimizu, K., Liang, Y., Sun, C., Jackson, C.R.M., and Saal, A.E. (2017) Parameterized lattice strain models for REE partitioning between amphibole and silicate melt. *American Mineralogist*, 102, 2254–2267, <https://doi.org/10.2138/am-2017-6110>.

Stosch, H.G. (1982) Rare earth element partitioning between minerals from anhydrous spinel peridotite xenoliths. *Geochimica et Cosmochimica Acta*, 46, 793–811, [https://doi.org/10.1016/0016-0016-7037\(82\)90031-X](https://doi.org/10.1016/0016-0016-7037(82)90031-X).

Sun, C. and Liang, Y. (2012) Distribution of REE between clinopyroxene and basaltic melt along a mantle adiabat: Effects of major element composition, water, and temperature. *Contributions to Mineralogy and Petrology*, 163, 807–823, <https://doi.org/10.1007/s00410-011-0700-x>.

— (2013) Distribution of REE and HFSE between low-Ca pyroxene and lunar picritic melts around multiple saturation points. *Geochimica et Cosmochimica Acta*, 119, 340–358, <https://doi.org/10.1016/j.gca.2013.05.036>.

— (2014) An assessment of subsolidus re-equilibration on REE distribution among mantle minerals olivine, orthopyroxene, clinopyroxene, and garnet in peridotites. *Chemical Geology*, 372, 80–91, <https://doi.org/10.1016/j.chemgeo.2014.02.014>.

Van Orman, J.A., Grove, T.L., and Shimizu, N. (2001) Rare earth element diffusion in diopside: Influence of temperature, pressure, and ionic radius, and an elastic model for diffusion in silicates. *Contributions to Mineralogy and Petrology*, 141, 687–703, <https://doi.org/10.1007/s00410-00100269>.

— (2002) Diffusion fractionation of trace elements during production and transport of melt in Earth's upper mantle. *Earth and Planetary Science Letters*, 198, 93–112, [https://doi.org/10.1016/S0012-821X\(02\)00492-2](https://doi.org/10.1016/S0012-821X(02)00492-2).

Wallace, M.E. and Green, D.H. (1991) The effect of bulk rock composition on the stability of amphibole in the upper mantle: Implications for solidus positions and mantle metasomatism. *Mineralogy and Petrology*, 44, 1–19, <https://doi.org/10.1007/BF01167097>.

Wang, C., Liang, Y., and Xu, W. (2021) Formation of amphibole-bearing peridotite and amphibole-bearing pyroxenite through hydrous melt-peridotite reaction and in situ crystallization: an experimental study. *Journal of Geophysical Research: Solid Earth*, 126, e2020JB019382, <https://doi.org/10.1029/2020JB019382>.

Wells, P.R. (1977) Pyroxene thermometry in simple and complex systems. *Contributions to Mineralogy and Petrology*, 62, 129–139, <https://doi.org/10.1007/BF00372872>.

Witt-Eickschen, G. and Harte, B. (1994) Distribution of trace elements between amphibole and clinopyroxene from mantle peridotites of the Eifel (western Germany): An ion-microprobe study. *Chemical Geology*, 117, 235–250, [https://doi.org/10.1016/0009-2541\(94\)90130-9](https://doi.org/10.1016/0009-2541(94)90130-9).

Witt-Eickschen, G. and O'Neill, H.S.C. (2005) The effect of temperature on the equilibrium distribution of trace elements between clinopyroxene, orthopyroxene, olivine, and spinel in upper mantle peridotite. *Chemical Geology*, 221, 65–101, <https://doi.org/10.1016/j.chemgeo.2004.04.005>.

Witt-Eickschen, G. and Seck, H.A. (1991) Solubility of Ca and Al in orthopyroxene from spinel peridotite: An improved version of an empirical geothermometer. *Contributions to Mineralogy and Petrology*, 106, 431–439, <https://doi.org/10.1007/BF00321986>.

Witt-Eickschen, G., Palme, H., O'Neill, H.S.C., and Allen, C. (2009) The geochemistry of the volatile trace elements As, Cd, Ga, In and Sn in the Earth's mantle: New evidence from in situ analyses of mantle xenoliths. *Geochimica et Cosmochimica Acta*, 73, 1755–1778, <https://doi.org/10.1016/j.gca.2008.12.013>.

Wood, B.J. and Banno, S. (1973) Garnet–orthopyroxene and orthopyroxene–clinopyroxene relationships in simple and complex systems. *Contributions to Mineralogy and Petrology*, 42, 109–124, <https://doi.org/10.1007/BF00371501>.

Wood, B.J. and Blundy, J.D. (1997) A predictive model for rare earth element partitioning between clinopyroxene and anhydrous silicate melt. *Contributions to Mineralogy and Petrology*, 129, 166–181, <https://doi.org/10.1007/s004100050330>.

— (2002) The effect of H₂O on crystal–melt partitioning of trace elements. *Geochimica et Cosmochimica Acta*, 66, 3647–3656, [https://doi.org/10.1016/S0016-7037\(02\)00935-3](https://doi.org/10.1016/S0016-7037(02)00935-3).

Wood, B.J. and Blundy, J. (2003) Trace element partitioning under crustal and uppermost mantle conditions: The influences of ionic radius, cation charge, pressure, and temperature. *Treatise on Geochemistry*, 2, 395–424, <https://doi.org/10.1016/B0-80-043751-6/02009-0>.

Xu, W., Yang, D., Gao, S., Pei, F., and Yu, Y. (2010) Geochemistry of peridotite xenoliths in early Cretaceous high-Mg# diorites from the central orogenic block of the North China Craton: The nature of Mesozoic lithospheric mantle and constraints on lithospheric thinning. *Chemical Geology*, 270, 257–273, <https://doi.org/10.1016/j.chemgeo.2009.12.006>.

Yao, L., Sun, C., and Liang, Y. (2012) A parameterized model for REE distribution between low-Ca pyroxene and basaltic melts with applications to REE partitioning in low-Ca pyroxene along a mantle adiabat and during pyroxenite-derived melt and peridotite interaction. *Contributions to Mineralogy and Petrology*, 164, 261–280, <https://doi.org/10.1007/s00410-012-0737-5>.

Zhang, Z.Y., Liu, C.Z., Liang, Y., Zhang, C., Liu, T., Zhang, W.Q., and Ji, W.B. (2022) Decoupled trace element and isotope compositions recorded in orthopyroxene and clinopyroxene in composite pyroxenite veins from the Xiuugugabu Ophiolite (SW Tibet). *Journal of Petrology*, 63, egac046, <https://doi.org/10.1093/petrology/egac046>.

Zhou, Q. (2014) Petrogenesis of wehrlite and pyroxenite xenoliths in early Cretaceous igneous Rocks from western Shandong, China. Ph.D. thesis, Jilin University, Changchun (in Chinese with English abstract).

MANUSCRIPT RECEIVED OCTOBER 6, 2022

MANUSCRIPT ACCEPTED FEBRUARY 22, 2024

ACCEPTED MANUSCRIPT ONLINE FEBRUARY 28, 2024

MANUSCRIPT HANDLED BY JULIE ROBERGE

Endnote:

¹Deposit item AM-24-118831. Online Materials are free to all readers. Go online, via the table of contents or article view, and find the tab or link for supplemental materials.